Research Article | Vol. 26, No. 20 | 1 Oct 2018 | OPTICS EXPRESS 26292
Optics EXPRESS

Multicascade-linked synthetic wavelength digital holography using an optical-comb-referenced frequency synthesizer

MASATOMO YAMAGIWA,[1,2] TAKEO MINAMIKAWA,[1,2] CLÉMENT TROVATO,[3,4,9] TAKAYUKI OGAWA,[2,3] DAHI GHAREAB ABDELSALAM IBRAHIM,[1,2,5] YUSUKE KAWAHITO,[6] RYO OE,[2,3] KYUKI SHIBUYA,[2,3] TAKAHIKO MIZUNO,[1,2] EMMANUEL ABRAHAM,[7] YASUHIRO MIZUTANI,[2,8] TETSUO IWATA,[1,2] HIROTSUGU YAMAMOTO,[2,9] KAORU MINOSHIMA,[2,10] AND TAKESHI YASUI[1,2,*]

[1]*Graduate School of Technology, Industrial and Social Sciences, Tokushima University, 2-1, Minami-Josanjima, Tokushima, Tokushima 770-8506, Japan*
[2]*JST, ERATO, MINOSHIMA Intelligent Optical Synthesizer Project, 2-1, Minami-Josanjima, Tokushima, Tokushima 770-8506, Japan*
[3]*Graduate School of Advanced Technology and Science, Tokushima University, 2-1, Minami-Josanjima, Tokushima, Tokushima 770-8506, Japan*
[4]*College of Sciences and Technology, University of Bordeaux, 351 cours de la Libération, Talence Cedex 33405, France*
[5]*Engineering and Surface Metrology Laboratory, National Institute of Standards, Tersa St., El haram, El Giza, Egypt*
[6]*Faculty of Science and Technology, Tokushima University, 2-1, Minami-Josanjima, Tokushima, Tokushima 770-8506, Japan*
[7]*Univ. Bordeaux, CNRS LOMA, UMR 5798, F-33400 Talence, France*
[8]*Graduate School of Engineering, Osaka University, 2-1, Yamadaoka, Suita, Osaka 565-0871, Japan*
[9]*Center for Optical Research and Education, Utsunomiya University, 7-1-2, Yoto, Utsunomiya, Tochigi 321-8585, Japan*
[10]*Graduate School of Informatics and Engineering, The University of Electro-Communications, 1-5-1 Chofugaoka, Chofu, Tokyo 182-8585, Japan*
**yasui.takeshi@tokushima-u.ac.jp*

Abstract: Digital holography (DH) is a promising method for non-contact surface topography because the reconstructed phase image can visualize the nanometer unevenness in a sample. However, the axial range of this method is limited to the range of the optical wavelength due to the phase wrapping ambiguity. Although the use of two different wavelengths of light and the resulting synthetic wavelength, i.e., synthetic wavelength DH, can expand the axial range up to several hundreds of millimeters, its axial precision does not reach sub-micrometer. In this article, we constructed a tunable external cavity laser diode phase-locked to an optical frequency comb, namely, an optical-comb-referenced frequency synthesizer, enabling us to generate multiple synthetic wavelengths within the range of 32 µm to 1.20 m. A multiple cascade link of the phase images among an optical wavelength (= 1.520 µm) and 5 different synthetic wavelengths (= 32.39 µm, 99.98 µm, 400.0 µm, 1003 µm, and 4021 µm) enables the shape measurement of a reflective millimeter-sized stepped surface with the axial resolution of 34 nm. The axial dynamic range, defined as the ratio of the axial range (= 2.0 mm) to the axial resolution (= 34 nm), achieves 5.9×10^5, which is larger than that of previous synthetic wavelength DH. Such a wide axial dynamic range capability will further expand the application field of DH for large objects with meter dimensions.

#337664 https://doi.org/10.1364/OE.26.026292
Journal © 2018 Received 3 Jul 2018; revised 18 Aug 2018; accepted 16 Sep 2018; published 25 Sep 2018

Optics EXPRESS

1. Introduction

Digital holography (DH) [1–4] has attracted attention as a three-dimensional (3D) imaging tool with nanometer axial resolution for biomedical imaging [5,6] and industrial inspection [7–9]. In DH, an interference fringe, formed by interfering diffracted light from an object with a reference light, is acquired using a digital imaging sensor such as a charge-coupled device (CCD) or a complementary metal-oxide semiconductor (CMOS) camera. Then, the amplitude and phase images of the object light can be reconstructed by a diffraction calculation of the acquired interference image with a computer. DH is featured by phase imaging, digital focusing, real-time imaging, and quantitative analysis. In particular, phase imaging enables nanometer axial resolution in the 3D shape measurement of transparent or reflective objects. When DH is performed using single-wavelength continuous wave (CW) laser light, the maximum axial range is limited within a half wavelength (λ/2) for reflective objects or a full wavelength (λ) for transparent objects due to the phase wrapping ambiguity. Although phase unwrapping processes can expand the maximum axial range [10], their adoption has been limited to a smooth shaped profile.

To extend the maximum axial range over a phase wrapping period of λ/2 or λ without the need for a phase unwrapping process, synthetic wavelength DH, referred to as SW-DH, has been proposed [11–15]. In this method, DH is performed at two different wavelengths (λ_1, λ_2), and then the synthetic wavelength Λ between them [= $(\lambda_1\lambda_2)/|\lambda_2-\lambda_1|$] is used to increase the maximum axial range up to $\Lambda/2$, which is larger than λ/2. However, since stable CW lasers operate at several discrete wavelengths of 532 nm, 612 nm, 633 nm, or 780 nm, the available Λ was limited to several microns. Even though three different wavelength lights were used for SW-DH, the maximum Λ value remained at approximately a few tens of microns [12,16]. One possible method to further increase Λ is the use of a tunable CW laser [17,18]. A distributed feedback laser diode is a stable tunable CW laser without mode hopping, and apply for the surface topography with the several-hundred-millimeter axial range; however, the axial precision remained at 10 μm. If multiple synthetic wavelengths with high stability and accuracy can be arbitrarily generated in the micrometer to meter range from a single light source and their phase images are cascade linked with each other, the maximum axial range will be significantly greater than the millimeter scale while maintaining the nanometer-scale axial resolution. It is anticipated that the resulting wide axial dynamic range DH will find many applications in the precise profilometry of large objects.

Widely and finely tunable CW light with high stability and accuracy in wavelength or optical frequency can be obtained by an optical-comb-referenced frequency synthesizer (OFS), which is a tunable external cavity laser diode (ECLD) phase-locked to an optical frequency comb (OFC) [19–21]. The OFC is composed of a series of optical frequency modes regularly spaced by a repetition frequency f_{rep} with a carrier-envelope offset frequency f_{ceo}. The OFC can be used as an optical frequency ruler by phase locking both f_{rep} and f_{ceo} to a frequency standard. By further phase locking the ECLD to one optical frequency mode of the OFC, the narrow linewidth, high stability, and high accuracy in the OFC are transferred to the ECLD, enabling the determination of the optical frequency based on the frequency standard. Furthermore, the optical frequency of the OFS can be tuned by switching the OFC mode phase-locked by the ECLD or by changing f_{rep} while maintaining the phase locking of the ECLD to the OFC mode. Such an OFS has been used for high-precision broadband spectroscopy in the near-infrared [19] and terahertz [20,21] regions. However, there have been no attempts to generate multiple synthetic wavelengths within the micrometer to millimeter range in SW-DH.

In this article, we demonstrate multiple synthetic wavelength DH (MSW-DH) using an OFS. The OFS is used for the acquisition of multiple phase images at five different synthetic wavelengths and an optical wavelength. The resulting series of phase images were coherently cascade linked for surface profilometry of a millimeter-stepped structure with nanometer axial resolution.

Optics EXPRESS

2. Principle of operation

2.1 Optical-comb-referenced frequency synthesizer (OFS)

Figure 1 shows the schematic diagram of the OFC and OFS. A vast number of OFC modes (freq. = ν_m) can be used as optical frequency markers in a broad spectral range based on the following equation

$$\nu_m = f_{ceo} + m f_{rep}, \tag{1}$$

where m is the mode number of the OFC. The parameter ν_m is given with an uncertainty of a frequency standard by determining m with an optical wavemeter while phase locking f_{ceo} and f_{rep} to the frequency standard. Next, we consider that the ECLD is phase-locked to the m-th OFC mode, namely, the OFS. The optical frequency of OFS ν_{ofs} is given by

$$\nu_{ofs} = \nu_m + f_{beat} = f_{ceo} + m f_{rep} + f_{beat}, \tag{2}$$

where f_{beat} is the beat frequency between the m-th OFC mode and ECLD light. If f_{beat} is phase-locked to the frequency standard, then the frequency uncertainty in the OFC is transferred to the ECLD, while the ECLD maintains its inherent characteristics such as wide wavelength tunability and moderate power usage. In other words, the OFS is traceable to the frequency standard via the OFC. More importantly from the viewpoint of MSW-DH, ν_{ofs} can be discretely tuned at a step of f_{rep} within the whole tunable range of the ECLD or the spectral range of the OFC by switching the m value in Eq. (2). Furthermore, ν_{ofs} can be tuned more precisely or more continuously by changing f_{rep} while maintaining the phase locking of the ECLD to the OFC mode. Here, we use the f_{rep}-step discrete tuning of the OFS for the generation of multiple synthetic wavelengths with a wide dynamic range.

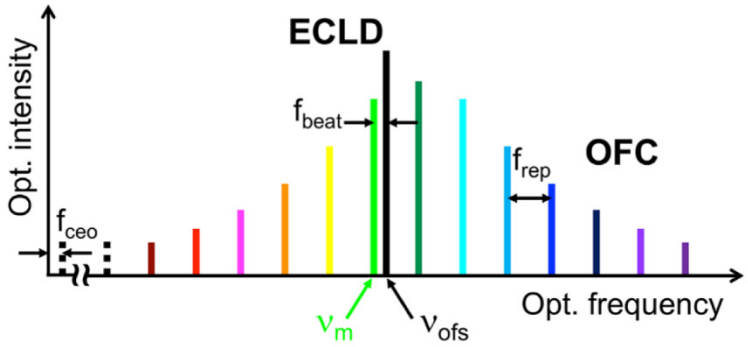

Fig. 1. Optical frequency comb and optical-comb-referenced frequency synthesizer.

2.2 Multicascade link of the synthetic wavelengths and optical wavelength

Principle of operation in SW-DH using two different wavelengths (λ_1, λ_2) is given in detail elsewhere [11–15]. The synthetic wavelength Λ is given by

$$\Lambda = \frac{\lambda_1 \lambda_2}{|\lambda_2 - \lambda_1|}, \tag{3}$$

In the phase-image-based shape measurement in a reflection configuration, the spatial height distribution $h(x, y)$ of a sample is given by

Optics EXPRESS

$$h(x,y)=\frac{\phi_{\lambda_1}(x,y)}{4\pi}\lambda_1+\frac{n_{\lambda_1}(x,y)}{2}\lambda_1=\frac{\phi_{\lambda_2}(x,y)}{4\pi}\lambda_2+\frac{n_{\lambda_2}(x,y)}{2}\lambda_2 \\ =\frac{\phi_{\Lambda}(x,y)}{4\pi}\Lambda+\frac{n_{\Lambda}(x,y)}{2}\Lambda=\frac{\phi_{\Lambda}(x,y)}{4\pi}\Lambda, \tag{4}$$

where $n_\lambda(x, y)$ and $\phi_\lambda(x, y)$ are respectively the spatial distributions of interference-fringe orders (integer) and phase values, corresponding to the number and a fraction of phase wrapping, at λ_1 or λ_2 and $n_\Lambda(x, y)$ and $\phi_\Lambda(x, y)$ are those at Λ, respectively. The function $\phi_\Lambda(x, y)$ is calculated by taking the difference of $\phi_\lambda(x, y)$ between λ_1 and λ_2. We here assumed that phase wrapping did not occur in $\phi_\Lambda(x, y)$; namely $n_\Lambda(x, y) = 0$. While $\phi_\lambda(x, y)$ and $\phi_\Lambda(x, y)$ can be measured within the phase range of 0 to 2π rad, $n_\lambda(x, y)$ cannot be directly determined due to the phase wrapping ambiguity. If $\phi_\Lambda(x, y)$ is used to determine $n_\lambda(x, y)$ and later $h(x, y)$ by the cascade link between λ and Λ, the maximum axial range is expanded to $\Lambda/2$ (typically, $\sim 10\lambda$) whereas the axial resolution of approximately $\lambda/100$ is maintained. The resulting axial dynamic range is expanded to 10^3. However, if $\phi_\Lambda(x, y)$ also undergoes phase wrapping, namely $n_\Lambda(x, y) \neq 0$, then $h(x, y)$ cannot be determined. The limited synthetic wavelengths (typically < a few tens of microns) by available CW lasers hinder the increase in the axial dynamic range.

The OFS can generate multiple synthetic wavelengths with different orders of magnitude ($= \Lambda_1 < \Lambda_2 < \bullet\bullet\bullet\bullet < \Lambda_{n-1} < \Lambda_n$) as multiple cascades, as shown in Fig. 2. When such a series of multiple synthetic wavelengths were used for MSW-DH together with λ, $h(x, y)$ is given by

$$h(x,y)=\frac{\phi_{\lambda}(x,y)}{4\pi}\lambda+\frac{n_{\lambda}(x,y)}{2}\lambda=\frac{\phi_{\Lambda_1}(x,y)}{4\pi}\Lambda_1+\frac{n_{\Lambda_1}(x,y)}{2}\Lambda_1 \\ =\frac{\phi_{\Lambda_2}(x,y)}{4\pi}\Lambda_2+\frac{n_{\Lambda_2}(x,y)}{2}\Lambda_2=\bullet\bullet\bullet\bullet\bullet \\ =\frac{\phi_{\Lambda_{n-1}}(x,y)}{4\pi}\Lambda_{n-1}+\frac{n_{\Lambda_{n-1}}(x,y)}{2}\Lambda_{n-1}=\frac{\phi_{\Lambda_n}(x,y)}{4\pi}\Lambda_n, \tag{5}$$

where $\phi_{\Lambda i}(x, y)$ and $n_{\Lambda i}(x, y)$ are respectively the spatial distributions of interference-fringe orders and phase values at Λ_i. If each $n_{\Lambda i}(x, y)$ value can be determined one after another from the longest synthetic wavelength Λ_n to the shortest synthetic wavelength Λ_1, then one can finally determine $n_\lambda(x, y)$ without errors. For example, in Eq. (5), the no-wrapping phase image $\phi_{\Lambda n}(x, y)$ obtained at the longest synthetic wavelength Λ_n is used to calculate $h_{\Lambda n}(x, y)$, where $h_{\Lambda n}(x, y)$ is $h(x, y)$ determined by Λ_n. Then, $h_{\Lambda n}(x, y)$ is used to determine $n_{\Lambda n-1}(x, y)$. Subsequently, the determined $n_{\Lambda n-1}(x, y)$ and the measured $\phi_{\Lambda n-1}(x, y)$ are used to determine $h_{\Lambda n-1}(x, y)$ more precisely. $n_{\Lambda i}(x, y)$ is given by

$$n_{\Lambda_i}(x,y)=INT\left[\frac{h_{\Lambda_{i+1}}(x,y)}{\Lambda_i/2}-\frac{\phi_{\Lambda_i}(x,y)}{2\pi}\right]. \tag{6}$$

By repeating a similar procedure from the longest to the shortest synthetic wavelength to the optical wavelength, $n_\lambda(x, y)$ can be determined correctly. By using such a multicascade link from Λ_n to λ, both the maximum axial range of $\Lambda_n/2$ and the axial resolution of $\lambda/100$ can be achieved at the same time. The resulting axial dynamic range becomes several orders of magnitude larger than the previous single SW-DH.

Optics EXPRESS

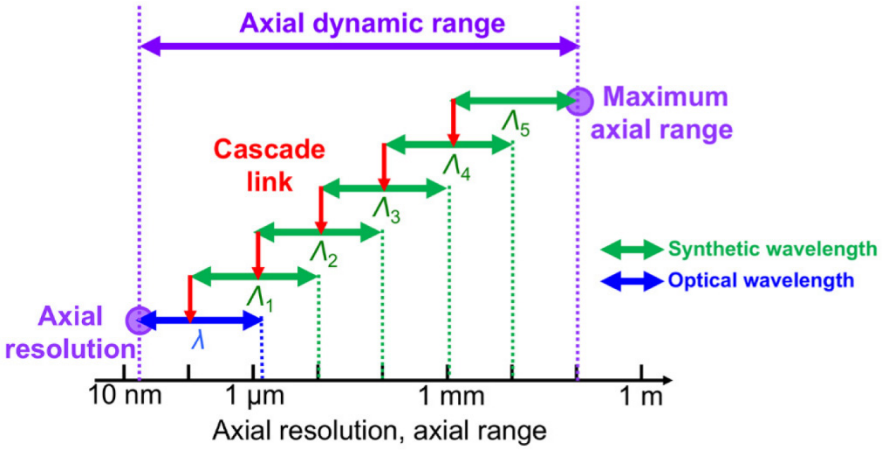

Fig. 2. Principle of operation in MSW-DH.

3. Methods

3.1 Experimental setup of the OFS

Figure 3(a) shows an experimental setup of the OFS, which is composed of an OFC and a tunable ECLD. We used a fiber OFC system (OFC; FC1500-250-WG, Menlo Systems GmbH, Martinsried, Germany, center wavelength = 1550 nm, spectral range = 1500 ~1600 nm, mean power = 60 mW, f_{rep} = 250 MHz, f_{ceo} = 20 MHz) for a frequency reference of a tunable ECLD (ECLD; LT-5001N, OptoComb, Inc., Tokyo, Japan, tuning range = 1520 nm ~1595 nm, mean power = 30 mW). The parameters f_{rep} and f_{ceo} were phase-locked to a rubidium frequency standard (Rb-FS; FS725, Stanford Research Systems, Sunnyvale, CA, USA, accuracy = 5×10^{-11} and instability = 2×10^{-11} at 1 s) by a frequency control system accompanied with the OFC. After polarization adjustment with pairs of a quarter waveplate (Q) and a half waveplate (H), a horizontally polarized beam from the OFC and a vertically polarized beam from the ECLD were spatially overlapped by a polarization beam splitter (PBS1), the polarization of both beams was directed at ± 45 degrees by another half waveplate, and their horizontal polarization components were extracted by another PBS (PBS2) for interference. After diffraction at a diffraction grating (GR25-0616, Thorlabs Inc., Newton, NJ, USA, 600 grooves/mm), an optical beat signal with f_{beat} between the ECLD beam and its most adjacent OFC mode was detected by an InGaAs photodetector (PD; PDA10CF-FC, Thorlab, bandwidth = 150 MHz). A proportional-integral servo controller (PI-SC; LB1005, Newport Corp., Irvine, CA, USA, bandwidth = 10 MHz) was used to control the current signal and the intracavity piezoelectric transducer of the ECLD so that f_{beat} was stabilized at 30 MHz by comparing f_{beat} with a reference frequency signal (freq. = 30 MHz) synthesized from a function generator (FG; 33210A, Keysight Technologies, Santa Rosa, CA, USA) using the same Rb-FS as an external time base. For tuning v_{ofs}, an m value was selected by changing the tilt angle of an internal grating in the ECLD.

3.2 Experimental setup of MSW-DH

We used an off-axis Michelson-type interferometer for MSW-DH, as shown in Fig. 3(b). The beam diameter of the output light from the OFS (mean power = 3 mW) was expanded to 54 mm by a pair of off-axis parabolic mirrors (OA-PM1, off-axis angle = 90°, diameter = 25.4 mm, focal length = 25.4 mm; OA-PM2, off-axis angle = 90°, diameter = 50.8 mm, focal length = 190.5 mm) and was fed into the Michelson interferometer. In the interferometer, the object beam was reflected by a cubic beam splitter (BS, reflection = 50%, transmittance = 50%), reflected at a sample, and then passed through the BS. The reference beam passed

Optics EXPRESS

through the BS, was reflected at a gold mirror (M, surface roughness = 63 nm), and then was reflected by the BS. Both beams were incident onto a cooled infrared CCD camera (Goldeye P-008, Allied Vision Technol. GmbH, Stadtroda, Germany, 320 x 256 pixels, pixel size = 30.0 µm × 30.0 µm, exposure time = 10 ms, digital output resolution = 14 bit) at an off-axis angle of 0.6°. This process resulted in the generation of interference patterns, namely, the digital hologram.

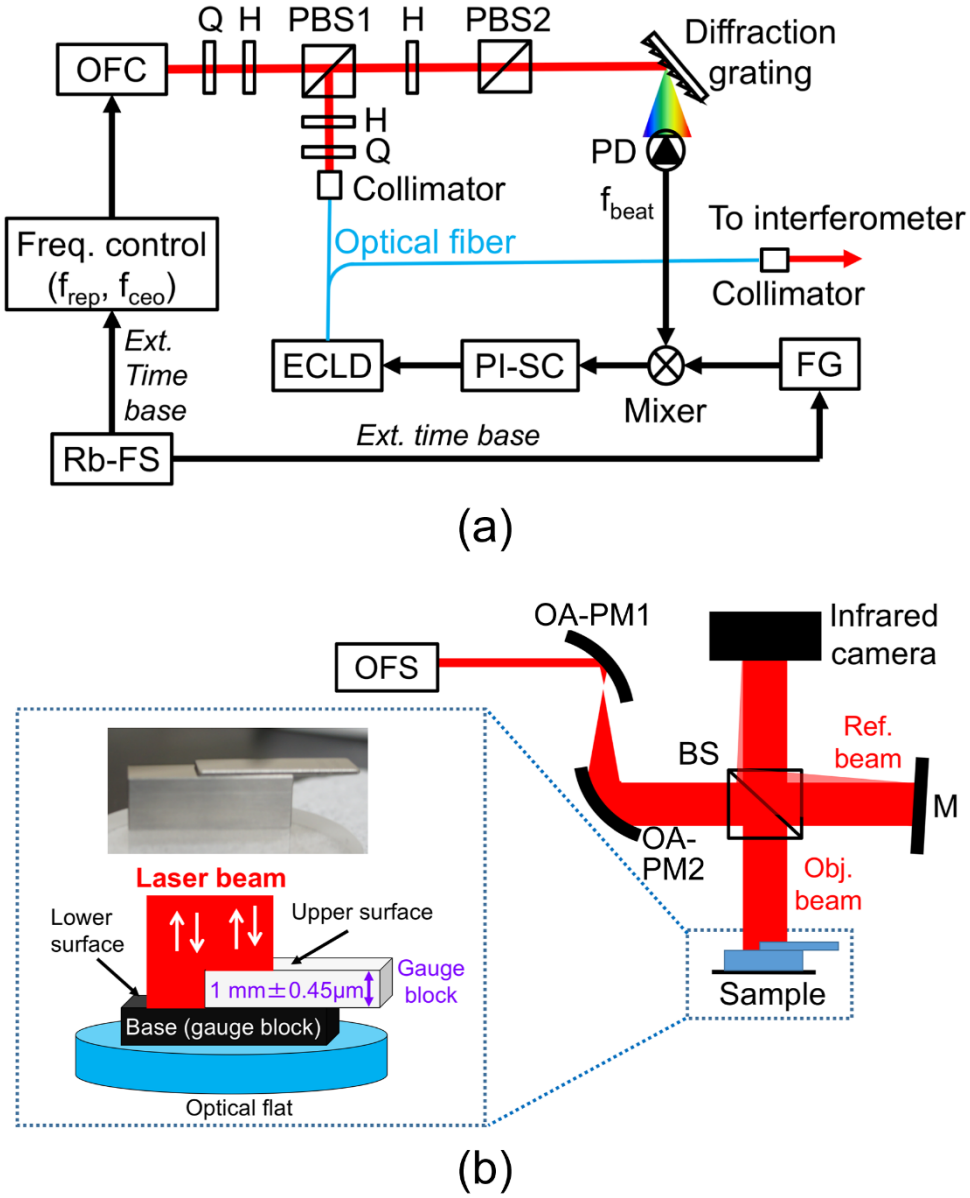

Fig. 3. Experimental setup of the OFS. OFC: optical frequency comb, ECLD: external cavity laser diode, Rb-FS rubidium frequency standard, PI-SC: proportional-integral servo controller, Hs: 1/2 waveplate, Qs:1/4 waveplate, PBS1 and PBS2: polarization beam splitter, PD: photodetector. (b) Experimental setup of the MSW-DH. OFS: optical-comb-referenced frequency synthesizer, OA-PM1 and OA-PM2: off-axis parabolic mirror, BS: beam splitter, and M: mirror. Inset in Fig. 3(b) shows a schematic drawing and a photograph of a sample with a stepped surface.

Optics EXPRESS

3.3 Angular spectrum method for the wavefront reconstruction of DH

We used an angular spectrum method (ASM) [22,23] for the wavefront propagation calculation. The angular spectrum $A(k_x, k_y; z)$ is given by the Fourier transform of the optical field $E(x, y; z)$. Therefore, the angular spectrum at the propagation distance $z = 0$ is given by

$$\begin{aligned} A_0(k_x, k_y) &= F\left[E_0(x_0, y_0)\right] \\ &= \iint E_0(x_0, y_0)\exp\left[-i(k_x x_0 + k_y y_0)\right]dx_0 dy_0. \end{aligned} \tag{7}$$

Next, the angular spectrum after propagation is specified as the product of $A_0(k_x, k_y)$ and a phase term for the propagation distance as follows

$$A(k_x, k_y; z) = A_0(k_x, k_y)\exp\left[iz\sqrt{k^2 - k_x^2 - k_y^2}\right]. \tag{8}$$

Finally, the optical field after propagation is obtained by the inverse Fourier formation of $A(k_x, k_y; z)$ as follows

$$\begin{aligned} E(x, y; z) &= F^{-1}\left[A(k_x, k_y; z)\right] \\ &= F^{-1}\left[F\left[E_0(x_0, y_0)\right]\exp\left[iz\sqrt{k^2 - k_x^2 - k_y^2}\right]\right]. \end{aligned} \tag{9}$$

The ASM has three advantages in wavefront reconstruction: First, the digital filtering in the spatial frequency domain eliminates the zero-order diffraction light and the conjugate first-order diffraction light images, both of which are unnecessary for the wavefront reconstruction. The spatial filtering of unnecessary components leads to the improved quality of reconstructed amplitude and phase images of the object. Second, the pixel size of the reconstructed image is the same as that of the obtained digital hologram. Third, the ASM has no limitation for the reconstruction distance z because the optical field is treated as a plane wave.

4. Results

4.1 Basic performance of the OFS

We first estimated the frequency fluctuation of ν_{ofs}. Since f_{ceo}, f_{rep}, and f_{beat} in Eq. (2) were phase-locked to the rubidium frequency standard, their frequency instability should be identical to that of the frequency standard. To evaluate the frequency instability of the rubidium frequency standard, we prepared two independent rubidium frequency standards with equivalent performance and used them for the frequency signal generation and the frequency signal measurement with an RF frequency counter (53220A, Keysight Technologies). The resulting frequency instability, calculated by Allan deviation, is shown in Fig. 4(a). From this frequency instability, we estimated the frequency fluctuation of f_{ceo}, f_{rep}, and f_{beat} with respect to gate time, as shown in Fig. 4(b). We further appended the frequency fluctuation of mf_{rep} when ν_{ofs} was fixed at 193.41505 THz or 1549.9955 nm by setting m to be 773,660. A comparison of f_{ceo}, mf_{rep}, and f_{beat} clearly indicated the frequency fluctuation of ν_{ofs} is determined by that of mf_{rep} due to the large number of m values. Importantly, the optical frequency fluctuation of the OFS is less than 1MHz at a gate time of 1 ms, which is several orders of magnitude smaller than that of CW lasers used in the previous research of SW-DH, due to the coherent frequency link with the frequency standard via the OFC.

The present OFS can generate single-mode CW light at a step of f_{rep} (= 250 MHz) or 1.9 pm within the wavelength range of 1520 nm ~1595 nm, that can be used for two wavelength lights with a wavelength difference of 1.9 pm to 75 nm. Figure 4(c) shows a relation between the wavelength difference $\Delta\lambda$ (= λ_2 - λ_1, λ_1 = 1520 nm) and the corresponding Λ [see Eq. (3)], indicating that the available Λ ranges from 32 μm to 1.20 m. The maximum Λ of 1.20 m is

Optics EXPRESS

three orders of magnitude larger than that in the previous study [18], highlighting the wide axial dynamic range in MSW-DH. We here generated five different synthetic wavelengths (Λ_1 = 32.38644 μm, Λ_2 = 99.97909 μm, Λ_3 = 400.0234 μm, Λ_4 = 1,002.524 μm, Λ_5 = 4021.204 μm) and a single optical wavelength (λ = 1.520302 μm) in the following demonstration.

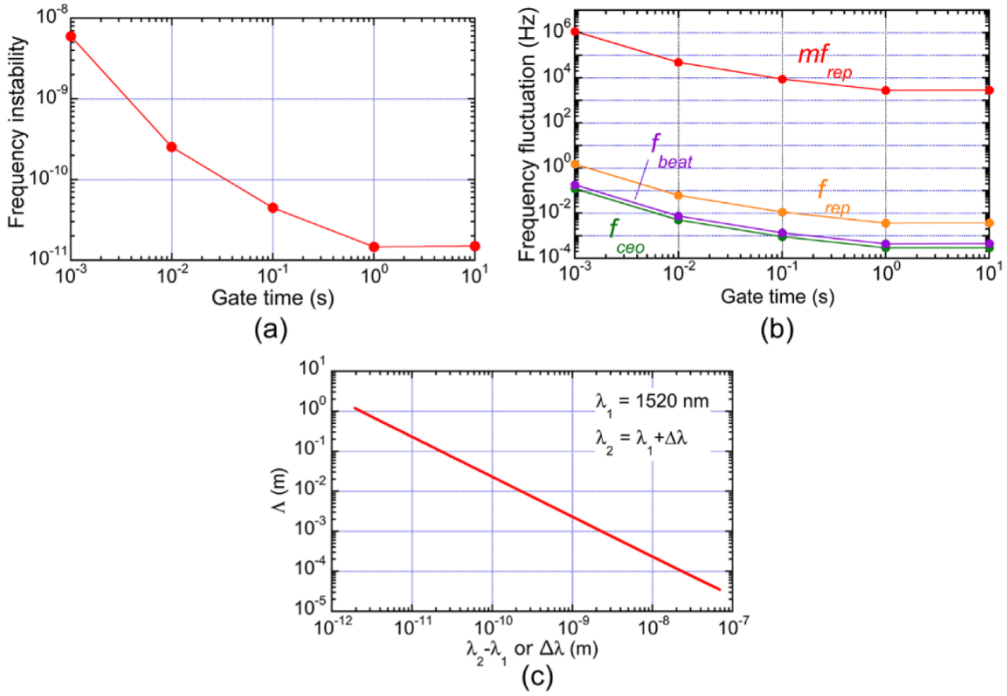

Fig. 4. Performance of the OFS. (a) Frequency instability of a rubidium frequency standard. (b) Frequency fluctuation of f_{ceo}, f_{rep}, f_{beat}, and mf_{rep} in the OFS. (c) Relation of the wavelength difference between two wavelength lights and the synthetic wavelength in the OFS.

4.2 Evaluation of the phase noise in MSW-DH

We evaluate the basic performance of the phase imaging by measuring a gauge block (164042, Mitutoyo, Kawasaki, Japan, thickness = 1 mm ± 0.45 μm, surface roughness = 21.6 nm) as a sample. We first evaluated spatial phase noise. We reconstructed the phase images of the sample at a reconstruction distance, z, of 134.2 mm using the ASM. Figures 5(a), 5(b), 5(c), 5(d), 5(e), and 5(f) show a series of phase images at λ, Λ_1, Λ_2, Λ_3, Λ_4, and Λ_5, respectively. Each phase image shows the spatial distribution of the phase value at the corresponding wavelength. We here defined the standard deviation of the spatial phase distribution $\phi_\lambda(x, y)$ or $\phi_{\Lambda i}(x, y)$ as a spatial phase noise, limiting the precision of the surface unevenness measurement. Figure 5(g) shows a comparison of the spatial phase noise among the optical wavelength λ and synthetic wavelengths Λ_1 ~Λ_5. Each phase image of Λ_i has a phase noise around 0.02 rad, which corresponds to a phase resolving power of around 1/314. The reason for the large phase noise at λ is mainly due to the surface roughness of the gauge block or the mirror in the referenced arm. By decreasing the wavelength from Λ_5 to λ, the precision of the surface unevenness measurement improved from 6.59 μm to 0.01 μm, as shown in Fig. 5(h).

We next evaluated temporal phase noise. The temporal phase noise was obtained by calculating the standard deviation of the phase values at the same pixel in 100 repetitive phase images with the same wavelength. The temporal phase noise depends on the robustness of the optical systems to an environmental disturbance, such as air turbulence or mechanical vibration, and hence is a critical factor to determine the uncertainty in the height measurement

Optics EXPRESS

based on the phase image. Figures 6(a), 6(b), 6(c), 6(d), 6(e), and 6(f) show the spatial distribution of the temporal phase noise at λ, Λ_1, Λ_2, Λ_3, Λ_4, and Λ_5, respectively. The similar distribution of temporal phase noise was confirmed in each phase image. Figure 6(g) compares the mean of the temporal phase noise among the optical wavelength λ and synthetic wavelengths $\Lambda_1 \sim \Lambda_5$. The temporal phase noise of around 0.1 rad, which corresponds to the phase resolving power of 1/63, respectively, was confirmed at each wavelength; this value is larger than the spatial phase noise due to the phase noise in the time domain. Figure 6(h) shows the corresponding uncertainty of the height measurement. From this result, we can determine the sample height with an axial resolution of 34 nm.

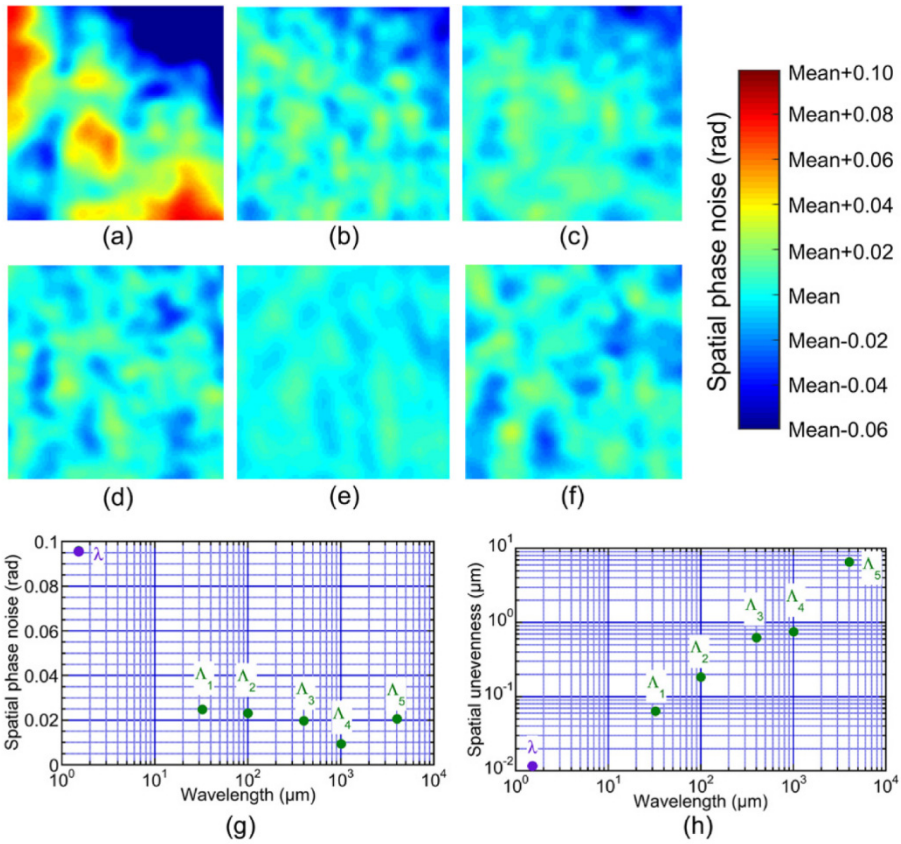

Fig. 5. Spatial phase noise of (a) λ (= 1.520302 μm), (b) Λ_1 (= 32.38644 μm), (c) Λ_2 (= 99.97909 μm), (d) Λ_3 (= 400.0234), (e) Λ_4 (= 1,002.524 μm), and (f) Λ_5 (= 4021.204 μm). Dependence of (g) spatial phase noise and (h) unevenness precision on wavelength.

Optics EXPRESS

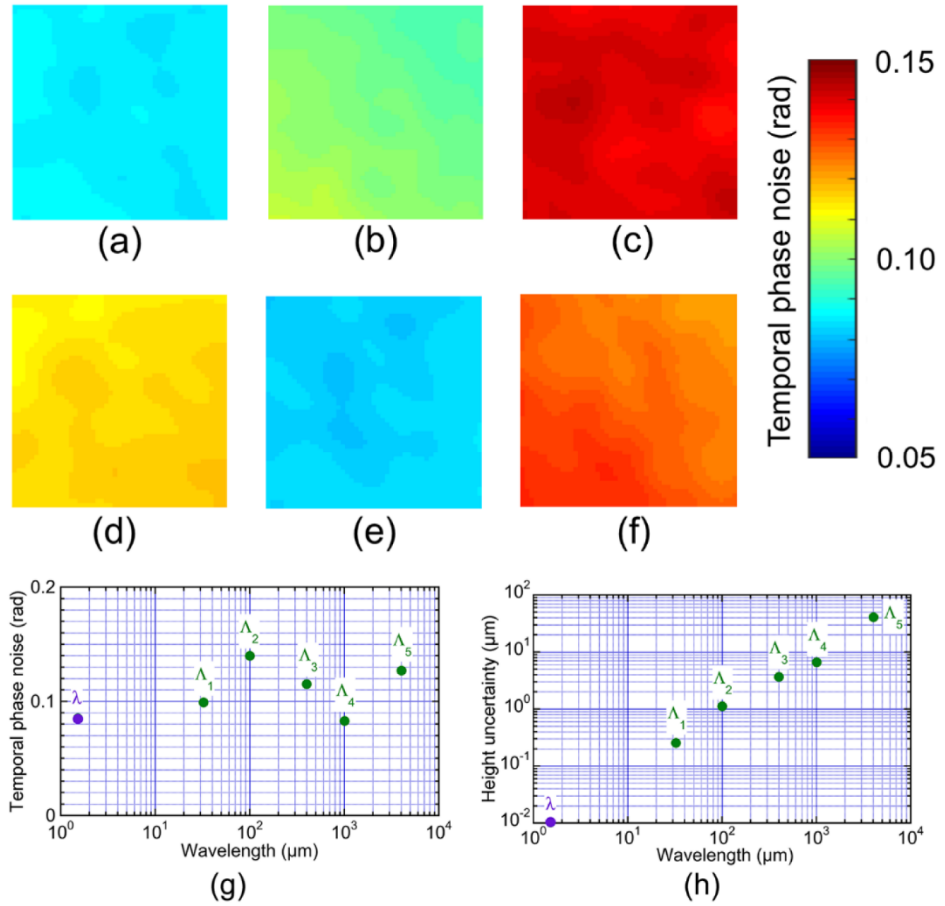

Fig. 6. Temporal phase noise of (a) λ (= 1.520302 μm), (b) Λ_1 (= 32.38644 μm), (c) Λ_2 (= 99.97909 μm), (d) Λ_3 (= 400.0234), (e) Λ_4 (= 1,002.524 μm), and (f) Λ_5 (= 4021.204 μm). Dependence of (g) temporal phase noise and (h) height uncertainty on wavelength.

4.3 3D Shape measurement of the stepped surface

Finally, we performed a 3D shape measurement of a stepped surface based on the cascade-linked phase images. We attached the same gauge block (164042, Mitutoyo, Kawasaki, Japan, thickness = 1 mm ± 0.45 μm, surface roughness = 21.6 nm) to another equivalent gauge block, as shown in the inset of Fig. 3(b). This stepped surface was used as a sample. Figures 7(a) and 7(b) show the spatial distributions of relative height for the upper surface and lower surface of the sample with respect to the number of cascade links (CLs). For example, no CLs just uses Λ_5 whereas full CLs is achieved by use of Λ_5, Λ_4, Λ_3, Λ_2, Λ_1, and λ. These results clearly indicated that the precision of the surface unevenness measurement was improved without error of $N_{\Lambda i}(x, y)$ or $N_\lambda(x, y)$ by the cascade link among the five different synthetic wavelengths and the optical wavelength.

To evaluate the uncertainty of the step height measurement, we repeated similar experiments for the same sample, and then determined the step height at each number of cascade links. Figure 7(c) shows the mean and standard deviation of the five repetitive measurements with respect to the number of cascade links. Finally, the step height was determined to be 999.969 ± 0.025 μm using the full CLs. Figure 7(d) shows the corresponding 3D shape of the stepped surface. The step difference determined by the MSW-

Optics EXPRESS

DH was in good agreement with the specification value of the thickness in the gauge block (= 1 mm ± 0.45 μm).

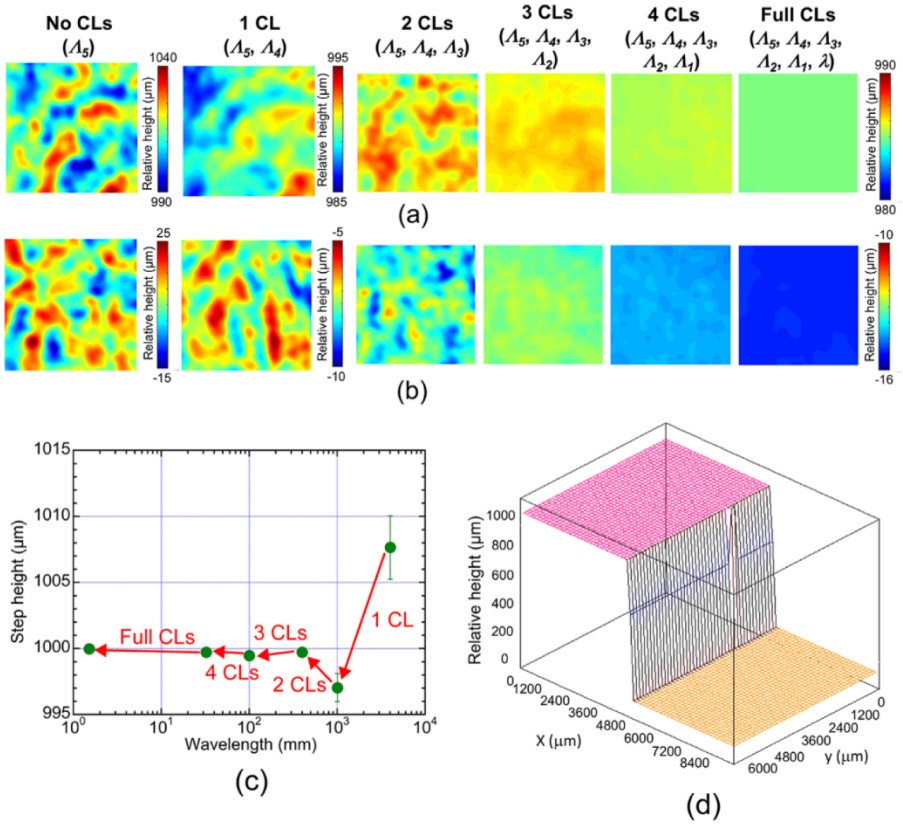

Fig. 7. Surface topography of a stepped surface sample. Spatial distributions of relative height for (a) an upper surface and (b) a lower surface with respect to the number of cascade links (CLs). The image size is 3 mm by 3 mm. (c) Improvement of the precision in the step height measurement with respect to the number of cascade links. (d) 3D profile of a 1-mm-step sample determined by the full cascaded link of a single optical wavelength and 5 synthetic wavelengths.

5. Discussion

We first discuss a possibility of a further enhancement in the axial dynamic range in the phase-image-based 3D shape measurement. In the demonstration above, an axial resolution of 34 nm was achieved within the axial range of 2 mm by using cascade link between 5 different synthetic wavelengths and an optical wavelength. However, the present OFS has a potential to increase the axial range up to 0.60 m. The resulting axial dynamic range was 1.7×10^8. Such a wide axial dynamic range is a distinctive feature in MSW-DH. It is important that there is still room to further expand the axial range. From the viewpoint of increased synthetic wavelength, the more precise tuning of v_{ofs} can be achieved by changing f_{rep} while maintaining the phase locking of the ECLD to the OFC mode. In this case, the minimum step is limited by the linewidth of the OFS [typically, 10 kHz at a gate time of 0.1 s in Fig. 4(b)]. Two wavelengths of light with an optical frequency difference of 10 kHz results in the generation of several tens kilometers in Λ, which is four orders of magnitude larger than the present maximum Λ.

We next discuss the possibility of real-time MSW-DH measurements. In this article, we applied five different synthetic wavelengths and one optical wavelength for MSW-DH. To

Optics EXPRESS

this end, we acquired holograms at six different optical wavelengths and calculated the phase images at synthetic wavelengths. Those holograms were acquired in order while ECLD was phase-locked to different mode of the OFC; the total acquisition time for the multiple holograms was typically a few minutes. In this article, we performed five cascade links among phase images with different wavelengths as a proof of concept; however, considering the temporal phase noise at Λ_i and λ, we can further reduce the number of cascade links while maintaining the same performance in MSW-DH, leading to the reduction of the total acquisition time. Furthermore, if the phase locking procedure of ECLD is excluded, the acquisition time of multiple holograms will be largely reduced. One possible method is use of a line-by-line pulse-shaping technique in the OFC [24]. In this case, a single OFC mode is arbitrarily and quickly extracted by the use of a spatial light modulator and then is directly used for the rapid generation of multiple synthetic wavelengths. If the selection of an arbitrary OFC mode is performed in synchronization with a frame timing in the infrared camera, all holograms required for MSW-DH will be acquired in real-time. Such an approach will enable us to achieve real-time MSW-DH. For more accessible source, electro-optics-modulator-based OFC [25] or micro-cavity OFC [26] is a possible candidate because of compactness, inexpensiveness, and/or no active stabilization.

One may wonder the similarity between MSW-DH and the ranging interferometer [27,28] because both can measure 3D shape of a specular object like a gauge block demonstrated in this article. In fact, the combination of OFC and multicascade-linked synthetic wavelength interferometry was effectively applied for the 3D shape measurement with the nanometer axial resolution and the meter axial range [27]. However, the calculation of phase retrieval based on Eqs. (7), (8), and (9) enables us to expand a sample of DH into a scattering object. Furthermore, such the phase retrieval calculation benefits from the improved lateral resolution even in the 3D shape measurement of a specular object. This is because the digital focusing based on the phase retrieval calculation can avoid the focusing problem in the lens-less configuration. On the other hand, the interferometry suffers from the diffraction of the sample edge, leading to the degraded lateral resolution. To highlight this point, we here compare the phase image between the DH and the interferometry. Figure 8(a) shows an interference image of the same 1-mm-stepped surface at λ (image size = 9.6 mm by 7.7 mm, pixel size = 320 pixels by 256 pixel) measured by the same system [see Fig. 3(b)]. A boundary between different steps appeared as a vertical black line, indicating somewhat blurred image across the boundary due to the diffraction of the sample edge. Then, we obtained the phase image of DH at λ by the ASM-based phase retrieval calculation (z = 134.2 mm) as shown in Fig. 8(b). We also obtained the phase image of the interferometry at λ by the Fourier transform method [28] as shown in Fig. 8(c). The similar phase image was confirmed in Figs. 8(b) and 8(c). To compare the lateral resolution in these phase images, we extracted the edge profile along an yellow line in Figs. 8(b) and 8(c). Figures 8(d) and 8(e) shows the edge profile of the phase image by the DH and the interferometry, respectively. The edge profile in DH was sharper than that in the interferometer due to the digital focusing. The digital focusing in DH further enables us to focus on each axial position even in a sample with the wide axial range over its depth of field; this is another advantage of DH over the interferometry because the axial range of a sample have to be within the depth of field in the interferometer to maintain its focusing.

Optics EXPRESS

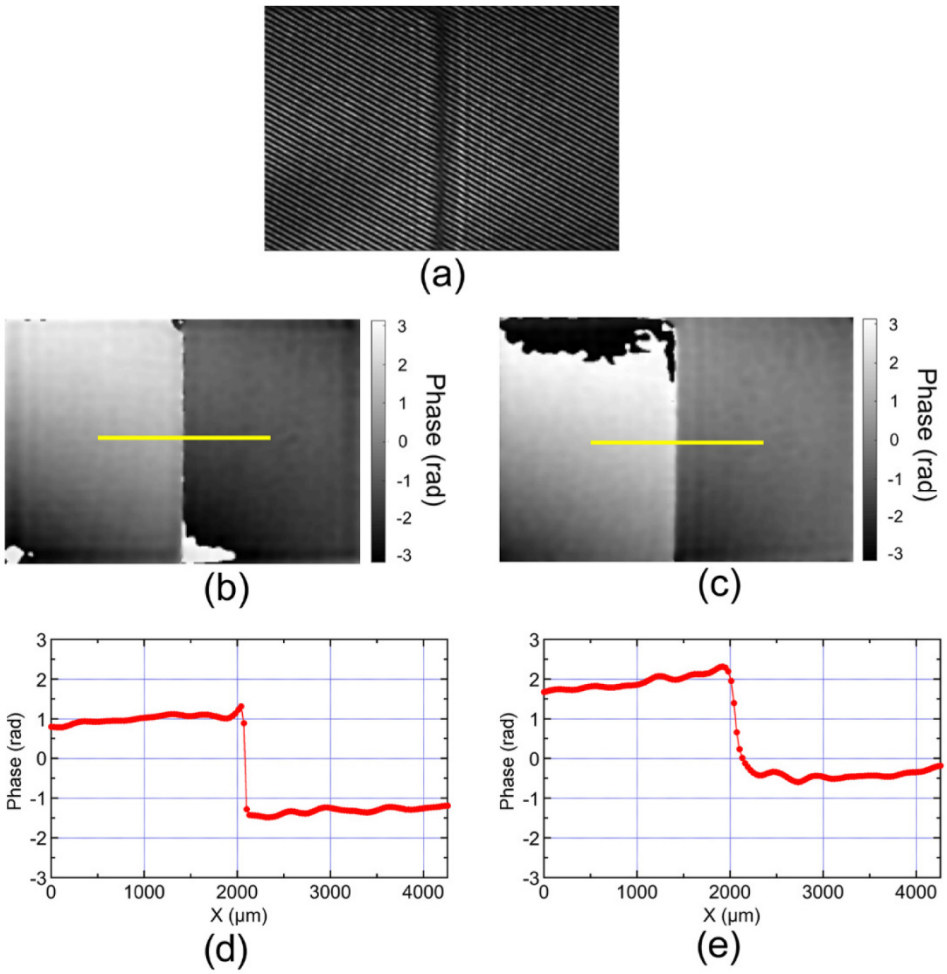

Fig. 8. Comparison of lateral resolution between DH and ranging interferometry. (a) Interference image of a 1-mm-stepped surface at λ (= 1.520302 μm). (b) Phase image calculated by the ASM-based phase retrieval calculation in DH (z = 134.2 mm). (c) Phase image calculated by the Fourier transform method in the interferometry. Comparison of edge profile between (d) the ASM-based phase retrieval calculation and (e) the Fourier transform method.

6. Conclusion

We demonstrated wide axial dynamic range MSW-DH using an OFS. The OFS has a potential to generate multiple synthetic wavelengths within the range of 32 μm to 1.20 m. The cascade link of phase images was demonstrated among a single optical wavelength and 5 synthetic wavelengths within the range from 1.5 μm to 4000 μm, and enabled us to achieve an axial resolution of 34 nm in a 3D shape measurement of a 1-mm-stepped surface with a precision of 25 nm. The wide axial dynamic range MSW-DH can be a powerful tool for surface topography of a specular object or a scattering object in industry, such as deformation measurement of large objects or evaluation of object shape.

Funding

Exploratory Research for Advanced Technology (ERATO), Japanese Science and Technology Agency (MINOSHIMA Intelligent Optical Synthesizer Project, JPMJER1304); Japan Society for the Promotion of Science (JSPS) (18K04981).

Optics EXPRESS

Acknowledgments

The authors thank Drs. Yasuaki Hori and Akiko Hirai at the National Institute of Advanced Industrial Science and Technology (AIST) for their help in the measurement of the gauge-block sample. We also acknowledge Dr. Yoshiaki Nakajima at the University of Electro-Communications and Dr. Sho Okubo at AIST for their help in the OFS.

References

1. S. Ulf and W. Jueptner, *Digital holography* (Springer Berlin Heidelberg, 2005).
2. K. M. Molony, B. M. Hennelly, D. P. Kelly, and T. J. Naughton, "Reconstruction algorithms applied to in-line Gabor digital holographic microscopy," Opt. Commun. **283**(6), 903–909 (2010).
3. E. Cuche, F. Bevilacqua, and C. Depeursinge, "Digital holography for quantitative phase-contrast imaging," Opt. Lett. **24**(5), 291–293 (1999).
4. I. Yamaguchi and T. Zhang, "Phase-shifting digital holography," Opt. Lett. **22**(16), 1268–1270 (1997).
5. P. Marquet, B. Rappaz, P. J. Magistretti, E. Cuche, Y. Emery, T. Colomb, and C. Depeursinge, "Digital holographic microscopy: a noninvasive contrast imaging technique allowing quantitative visualization of living cells with subwavelength axial accuracy," Opt. Lett. **30**(5), 468–470 (2005).
6. B. Kemper and G. von Bally, "Digital holographic microscopy for live cell applications and technical inspection," Appl. Opt. **47**(4), A52–A61 (2008).
7. B. Javidi and E. Tajahuerce, "Three-dimensional object recognition by use of digital holography," Opt. Lett. **25**(9), 610–612 (2000).
8. V. Kebbel, H.-J. Hartmann, and W. P. O. Jüptner, "Application of digital holographic microscopy for inspection of micro-optical components," Proc. SPIE **4398**, 189–199 (2001).
9. Y. Emery, E. Cuche, F. Marquet, N. Aspert, P. Marquet, J. Kuhn, M. Botkine, T. Colomb, F. Montfort, F. Charriere, and C. Depeursinge, "Digital holography microscopy (DHM): fast and robust systems for industrial inspection with interferometer resolution," Proc. SPIE **5856**, 930–938 (2005).
10. M. A. Schofield and Y. Zhu, "Fast phase unwrapping algorithm for interferometric applications," Opt. Lett. **28**(14), 1194–1196 (2003).
11. J. Gass, A. Dakoff, and M. K. Kim, "Phase imaging without 2π ambiguity by multiwavelength digital holography," Opt. Lett. **28**(13), 1141–1143 (2003).
12. D. Parshall and M. K. Kim, "Digital holographic microscopy with dual-wavelength phase unwrapping," Appl. Opt. **45**(3), 451–459 (2006).
13. J. Kühn, T. Colomb, F. Montfort, F. Charrière, Y. Emery, E. Cuche, P. Marquet, and C. Depeursinge, "Real-time dual-wavelength digital holographic microscopy with a single hologram acquisition," Opt. Express **15**(12), 7231–7242 (2007).
14. A. Khmaladze, M. Kim, and C. M. Lo, "Phase imaging of cells by simultaneous dual-wavelength reflection digital holography," Opt. Express **16**(15), 10900–10911 (2008).
15. Z. Wang, J. Jiao, W. Qu, F. Yang, H. Li, A. Tian, and A. Asundi, "Linear programming phase unwrapping for dual-wavelength digital holography," Appl. Opt. **56**(3), 424–433 (2017).
16. C. J. Mann, P. R. Bingham, V. C. Paquit, and K. W. Tobin, "Quantitative phase imaging by three-wavelength digital holography," Opt. Express **16**(13), 9753–9764 (2008).
17. Y. Li, W. Xiao, and F. Pan, "Multiple-wavelength-scanning-based phase unwrapping method for digital holographic microscopy," Appl. Opt. **53**(5), 979–987 (2014).
18. V. Lédl, P. Psota, F. Kaván, O. Matoušek, and P. Mokrý, "Surface topography measurement by frequency sweeping digital holography," Appl. Opt. **56**(28), 7808–7814 (2017).
19. H. Takahashi, Y. Nakajima, H. Inaba, and K. Minoshima, "Ultra-broad absolute-frequency tunable light source locked to a fiber-based frequency comb," in *Conference on Lasers and Electro-Optics* (2009), paper CTuK4.
20. T. Yasui, H. Takahashi, K. Kawamoto, Y. Iwamoto, K. Arai, T. Araki, H. Inaba, and K. Minoshima, "Widely and continuously tunable terahertz synthesizer traceable to a microwave frequency standard," Opt. Express **19**(5), 4428–4437 (2011).
21. Y.-D. Hsieh, H. Kimura, K. Hayashi, T. Minamikawa, Y. Mizutani, H. Yamamoto, T. Iwata, H. Inaba, K. Minoshima, F. Hindle, and T. Yasui, "Terahertz frequency-domain spectroscopy of low-pressure acetonitrile gas by a photomixing terahertz synthesizer referenced to dual optical frequency combs," J. Infrared Millim. Terahertz Waves **37**(9), 903–915 (2016).
22. M. K. Kim, L. Yu, and C. J. Mann, "Interference techniques in digital holography," J. Opt. A, Pure Appl. Opt. **8**(7), S518–S523 (2006).
23. T. Poon and J. Liu, *Introduction to Modern Digital Holography with MATLAB* (Cambridge University, 2014).
24. Z. Jiang, D. S. Seo, D. E. Leaird, and A. M. Weiner, "Spectral line-by-line pulse shaping," Opt. Lett. **30**(12), 1557–1559 (2005).
25. I. Morohashi, T. Sakamoto, H. Sotobayashi, T. Kawanishi, and I. Hosako, "Broadband wavelength-tunable ultrashort pulse source using a Mach-Zehnder modulator and dispersion-flattened dispersion-decreasing fiber," Opt. Lett. **34**(15), 2297–2299 (2009).
26. P. Del'Haye, A. Schliesser, O. Arcizet, T. Wilken, R. Holzwarth, and T. J. Kippenberg, "Optical frequency comb generation from a monolithic microresonator," Nature **450**(7173), 1214–1217 (2007).

Optics EXPRESS

27. Y.-S. Jang, G. Wang, S. Hyun, H. J. Kang, B. J. Chun, Y.-J. Kim, and S.-W. Kim, "Comb-referenced laser distance interferometer for industrial nanotechnology," Sci. Rep. **6**(1), 31770 (2016).
28. W. Zhang, H. Wei, H. Yang, X. Wu, and Y. Li, "Comb-referenced frequency-sweeping interferometry for precisely measuring large stepped structures," Appl. Opt. **57**(5), 1247–1253 (2018).